Topological Two-Dimensional Floquet Lattice on a Single Superconducting Qubit

Daniel Malz[1,2,*] and Adam Smith[3,4,5,*]

[1]*Max Planck Institute for Quantum Optics, Hans-Kopfermann-Straße 1, D-85748 Garching, Germany*
[2]*Munich Center for Quantum Science and Technology, Schellingstraße 4, D-80799 München, Germany*
[3]*Department of Physics, TFK, Technische Universität München, James-Franck-Straße 1, D-85748 Garching, Germany*
[4]*School of Physics and Astronomy, University of Nottingham, Nottingham, NG7 2RD, United Kingdom*
[5]*Centre for the Mathematics and Theoretical Physics of Quantum Non-Equilibrium Systems, University of Nottingham, Nottingham, NG7 2RD, United Kingdom*

(Received 11 December 2020; revised 1 March 2021; accepted 22 March 2021; published 23 April 2021)

Current noisy intermediate-scale quantum (NISQ) devices constitute powerful platforms for analog quantum simulation. The exquisite level of control offered by state-of-the-art quantum computers make them especially promising to implement time-dependent Hamiltonians. We implement quasiperiodic driving of a single qubit in the IBM Quantum Experience and thus experimentally realize a temporal version of the half-Bernevig-Hughes-Zhang Chern insulator. Using simple error mitigation, we achieve consistently high fidelities of around 97%. From our data we can infer the presence of a topological transition, thus realizing an earlier proposal of topological frequency conversion by Martin, Refael, and Halperin. Motivated by these results, we theoretically study the many-qubit case, and show that one can implement a wide class of Floquet Hamiltonians, or time-dependent Hamiltonians in general. Our study highlights promises and limitations when studying many-body systems through multifrequency driving of quantum computers.

DOI: 10.1103/PhysRevLett.126.163602

Introduction.—Noisy intermediate-scale quantum (NISQ) computers may not yet offer fully fault-tolerant quantum computing facilities, but they nevertheless constitute a versatile experimental platform with the potential for fundamental research, small-scale computation or quantum simulation [1]. The typical model of a quantum computer is that of a quantum circuit, which is a sequence of gates applied to the qubits [2]. In principle, the time evolution of any many-body quantum systems can be simulated by applying a Trotterization, which turns continuous time evolution into a discrete local quantum circuit [3]. This results in a digital quantum simulation, which has been benchmarked for a range of different models on existing quantum computers [4–7].

In superconducting circuits, the currently leading technology, quantum circuits are constructed from a set of available gates, which correspond to a set of carefully calibrated microwave pulses applied to its input ports [8]. The abstraction into quantum circuits hides the complexity of the underlying many-body system, whose continuous evolution offers exciting directions in *analog* quantum simulation [9,10], which potentially incurs significantly less overhead. This perspective has been explored in a series of theoretical and experimental works [11–15]. If the intrinsic many-body nature of quantum computers is combined with the capacity to apply essentially arbitrary drives, they may serve also as powerful analog quantum simulators for very large classes of time-dependent Hamiltonians.

The evolution under time-dependent Hamiltonians is incredibly rich and exhibits many novel phenomena, even at the level of individual qubits. A particular example is the temporal topological transition that occurs in the presence of quasiperiodic driving, theoretically predicted by Martin, Refael, and Halperin in 2017 [16]. Using a Floquet treatment of the driven qubit, the dynamics is related to the properties of a two-dimensional lattice model, the half-Bernevig-Hughes-Zhang (BHZ) Chern insulator [17]. As a function of time, the driven qubit explores the whole Brillouin zone, which causes the work done by the two drives to be quantized and proportional to the integer Chern number, which is determined by the parameters in the drives. Recently, temporal topology has been classified, analogously to the classification of topological insulators [18], and extension to larger systems, such as spin-resonator systems [19], or two-qubit systems with interactions [20] have been proposed. While quasiperiodic driving typically maps to systems without boundary, one can, in principle, also introduce boundaries through quantum feedback [21].

In this work we experimentally demonstrate this temporal topological behavior of a single qubit on an existing quantum device, using continuous driving, implemented with the fine-grained access offered by QISKIT pulse [22]. Choosing a specific driving with two incommensurate frequencies, we observe a topological transition in the temporal dynamics of the qubit, finding good agreement with simulations. Despite achieving high fidelities of around 97% after error mitigation, the Chern number inferred from the measured frequency conversion shows much larger errors. We develop a simple noise model that explains and reproduces this effect.

Motivated by this experiment, we theoretically derive the class of Hamiltonians that can readily be implemented on state-of-the-art quantum computers. As one concrete example, this offers an exciting perspective to study strongly interacting Floquet systems [23–27] with an exquisite level of control. Site-selective control as well as high-fidelity single-site readout confers quantum computers certain advantage over other quantum simulators based on light [28] or ultracold atoms [29], making them ideally suited for the analog quantum simulation of generic many-body time-dependent Hamiltonians.

Theoretical description.—In quantum computers based on superconducting transmonlike qubits [30,31], the Hamiltonian describing a single qubit can be cast in the form of a Duffing oscillator with driving

$$H(t) = \omega_0 a^\dagger a + U a^\dagger a^\dagger a a + (a + a^\dagger) D(t). \tag{1}$$

The qubit frequency is denoted ω_0 and U quantifies the anharmonicity that separates the lowest two levels that define the qubit from the higher levels of the superconducting circuit. The ideal drive signal is parametrized as [22]

$$D(t) = \frac{\Omega_{\max}}{2} \mathrm{Re}[e^{i(\omega_0 + \Delta_c)t} d(t)], \tag{2}$$

where $\Omega_{\max}$ denotes the maximum Rabi frequency attainable in the system, and $\omega_0 + \Delta_c$ is the carrier frequency. In the following, we choose the detuning $\Delta_c = 0$. Anticipating our later interpretation as a spin-1/2 particle in a time-dependent field, we parameterize the dimensionless drive shape $d(t) \in \mathbb{C}, |d(t)| \leq 1$ in terms of the dimensionless magnetic field $\tilde{h}_+(t) = \tilde{h}_x(t) + i\tilde{h}_y(t)$

$$d(t) \equiv \tilde{h}_+(t) \exp i\phi(t), \qquad \phi(t) = -2\Omega_{\max} \int_0^t \tilde{h}_z(t')dt'. \tag{3}$$

To treat the system as a qubit, the maximum drive strength needs to be much weaker than the anharmonicity $\Omega_{\max} \ll U$. Assuming this is fulfilled, applying a rotating-wave approximation and passing into a frame rotating with respect to the time-dependent Hamiltonian $H_z(t) = (\omega_0/2 - h_z(t))\sigma_z$, we rewrite Eq. (1) as [32]

$$H_{\mathrm{spin}}(t) = \vec{h}(t) \cdot \vec{\sigma}. \tag{4}$$

Note the subtlety in the chosen rotating frame. Instead of changing the qubit frequency in the lab frame, we reparametrize time by passing into a rotating frame with respect to $H_z(t)$. This constitutes a continuous version of virtual Z gates [35].

Topological frequency conversion.—Given Eq. (4), we can now realize the proposal by Martin *et al.* [16]. We apply the quasiperiodic time-dependent magnetic field

$$\begin{aligned} H(t) = \eta\{&\sin(\omega_1 t + \phi_1)\sigma_x + \sin(\omega_2 t + \phi_2)\sigma_y \\ &+ [M - \cos(\omega_1 t + \phi_1) - \cos(\omega_2 t + \phi_2)]\sigma_z\}, \end{aligned} \tag{5}$$

where the ratio ω_2/ω_1 should be irrational. In the following, we set $\omega_2/\omega_1 = (1 + \sqrt{5})/2$. We consider the model in the strong drive limit, i.e., $\eta \gg \omega_1, \omega_2$. In this limit, a Floquet ansatz reveals a direct connection to the two-dimensional half-BHZ Chern insulator [17] with a constant electric field applied [16,32]. In the strong-drive limit, the electric field is weak and leads to a slow adiabatic evolution of the initial wavepacket through the Brillouin zone. During this evolution, which explores the whole Brillouin zone, the system effectively measures the Chern number, which results in a topologically quantized energy pumping rate from one drive to the other [16]

$$\pi \frac{(W_1 - W_2)}{\omega_1 \omega_2 T} = C, \tag{6}$$

where W_i is the work done by the ith drive, defined below [Eq. (8)]. As a function of M, the system undergoes a topological transition in which the Chern number changes.

To determine the pumping rate experimentally, we measure the work done by each of the drives. If we first split the Hamiltonian into the two contributions from each drive,

$$H(t) = h_1(t) + h_2(t) + \eta M \sigma_z, \tag{7}$$

then the work done by each drive over a period T is given by

$$W_i(T) = \int_0^T dt \langle \Psi(t)| \frac{dh_i(t)}{dt} |\Psi(t)\rangle, \tag{8}$$

where $|\Psi(t)\rangle$ is the state of the qubit at time t evolving under the time-dependent Schrödinger equation $i\partial_t|\Psi(t)\rangle = H(t)|\Psi(t)\rangle$, where $|\Psi(t=0)\rangle$ is chosen to be an instantaneous eigenstate of $H(t=0)$.

Experiment.—Our experimental protocol consists of four main pulse sequences. First, we initialize the qubit in the

instantaneous eigenstate of Hamiltonian Eq. (5) at $t = 0$. This is achieved using an IBM calibrated pulse sequence to perform a general qubit rotation. Second, the main pulse sequence implements the time-dependent Hamiltonian (5), with the drive parametrized as in Eq. (2). We perform experiments with different drive lengths of up to 20 μs to obtain 800 data points. Third, we apply an IBM calibrated pulse to change the basis. For each drive length, we rotate into the X, Y, and Z bases in order to perform full state tomography. Finally, we perform single-shot projective measurements of the qubit using an IBM pre-calibrated readout pulse sequence. We average over 8192 shots for each observable corresponding to a statistical error of approximately 1%.

We fix $\omega_2 = \varphi\omega_1$, where $\varphi = (1+\sqrt{5})/2$ is the golden ratio. Ideally, we would be like to set the ratio ω_1/η as small as possible, to get as close as possible to adiabatic evolution. However, due to the finite coherence time $\tau \gtrsim 100$ μs of the IBM Q device, we must choose $\omega_1^{-1} \ll \tau$. In terms of the maximum Rabi frequency $\Omega_{\max}$, we choose $\eta = 0.9\Omega_{\max}$, in order to avoid driving transitions to higher excited states. Using numerical simulations we found the best compromise was to choose a total simulation time of 20 μs and set $\omega_1 = 0.125\eta$, which corresponds to $\omega_1^{-1} \approx 240$ ns. In order to improve the fidelity of our results we start the drive with a linear ramp of the drive frequencies ω_1, ω_2 over a period of 444 ns. This reduces transient effects and reduces high-frequency Rabi oscillations seen in the simulation results. The single-qubit IBM device we used, codenamed armonk, had qubit frequency $\omega_0 \approx 4.97$ GHz and maximum Rabi frequency of $\Omega_{\max} \approx 36.9$ MHz.

With the above experimental protocol we measure the observables in the frame rotating with the qubit frequency. Since the Hamiltonian Eq. (4) is only realized in a given time-dependent reference frame, we must additionally perform a virtual-Z rotation, which we achieve by post-processing the data to apply the rotation

$$\begin{aligned}\langle\sigma_x\rangle_{\text{rotating}} &= \cos\phi(t)\langle\sigma_x\rangle + \sin\phi(t)\langle\sigma_y\rangle,\\ \langle\sigma_y\rangle_{\text{rotating}} &= -\sin\phi(t)\langle\sigma_x\rangle + \cos\phi(t)\langle\sigma_y\rangle,\end{aligned} \tag{9}$$

where $\phi(t)$ is given in Eq. (3). When post-processing the data, we additionally mitigate some of the errors due to decoherence and measurement error by projecting the measured qubit density matrix onto the Bloch sphere. We find that this method of error mitigation improves quantitative agreement with numerical simulations in all cases we considered. This effectively removes the effects of the dominant depolarizing channel [36]. With this error mitigation strategy, the average fidelity across all experiments is 0.971 (excluding $M = 1.7$, 2.3 due to strong diabatic effects that arise due to the proximity to the gap closing at $M = 2$ [32]).

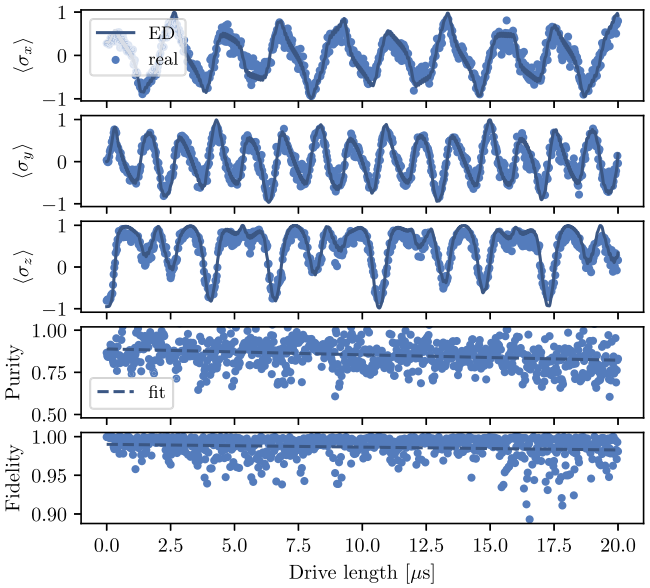

FIG. 1. Tomography data for $M = 1$, $\omega_1 = 0.125$. The top three panels compare experimentally measured Pauli expectation values against exact numerical simulation. We also show the purity of the measured state, which we fit by the function $1/2 + ae^{-t/\lambda}$, where $a = 0.387$ and $\lambda \approx 109$ μs is compatible with the device coherence time as measured by IBM. Note that $a < 0.5$ as the measurement sequence take a finite time, such that the qubit has lost purity even when the simulation time is zero. The bottom panel shows the fidelity $\mathcal{F} = |\langle\psi|\phi\rangle|^2$ between the measured state projected onto the Bloch sphere, $|\psi\rangle$, and the numerically simulated state, $|\phi\rangle$. We fit the fidelity with $ae^{-t/\xi}$, where $a \approx 0.99$ and $\xi \approx 2.71$ ms, which verifies the effectiveness of error mitigation by projecting onto the Bloch sphere.

The experimental tomography data is shown in Fig. 1 for $M = 1$, which closely matches the exact numerical simulation. From this data we can also compute the purity of the measured state $\mathrm{Tr}(\rho^2)$, also shown in Fig. 1. The measured purity is less than one due to decoherence over the course of the experiment along with the significant ~3% measurement error. Fitting the purity with an exponential decay, we extract a decoherence time of $\lambda \approx 109$ μs (at $M = 1$), which is consistent with the $T_1, T_2 \gtrsim 100$ μs decoherence times measured by IBM.

Results.—To obtain the work done by each drive [Eq. (8)], we first compute $\langle dh_i(t)/dt\rangle = d\vec{h}_i(t)/dt \cdot \langle\vec{\sigma}\rangle$ from the data. We then perform the integration in Eq. (8) numerically. Figure 2 shows the experimental results for the work done, for the case of $M = 1$. This corresponds to a phase of the BHZ model with Chern number $C = -1$, resulting in an average linear decrease (increase) of W_1 (W_2). The experimental results are in good quantitative agreement with numerical simulations. Furthermore, by fitting a linear curve to this data using least-squares regression, the slope is in close agreement to that predicted by Eq. (6).

Figure 3 shows the extracted Chern number for a range of values of M, compared against numerical simulations of

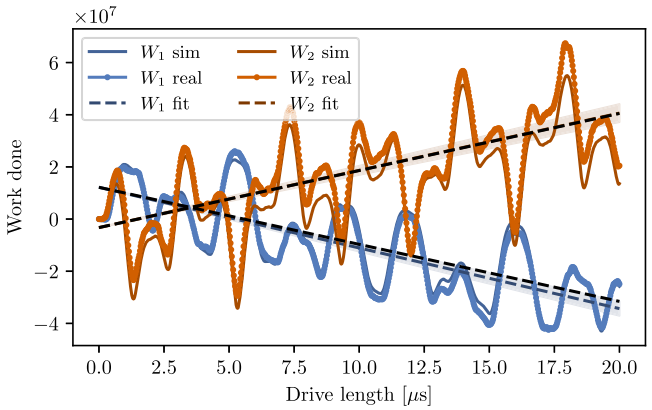

FIG. 2. Work done by the two incommensurate drives, calculated using Eq. (8). The experimental data for $M = 1, \omega_1 = 0.125$ measured at 800 points is compared with a numerical simulation of the same setup. The experimental data is fitted with a line (colored dashed lines) using least-squares regression, for which the 95% confidence interval for the slope is shown as the colored region. The expected slope is shown as black dashed lines.

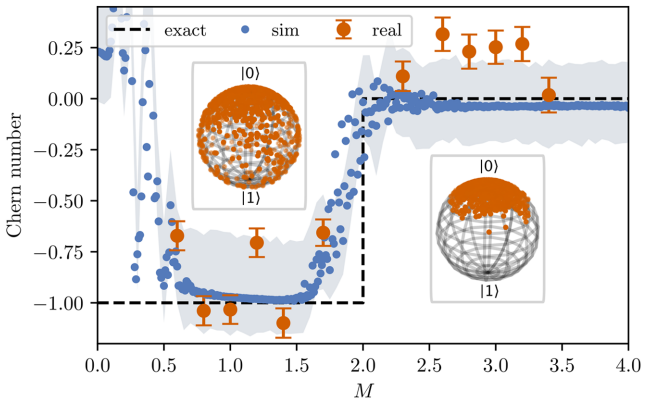

FIG. 3. Experimentally extracted Chern number as a function of M. The Chern number is extracted from the linear least-squares regression fit to the work done by each drive, and using Eq. (6). The error bars correspond to the 95% confidence intervals for the fit. The experimental data are compared against the numerical simulation of the same setup (blue dots) and with the exact value of the Chern number for the corresponding phase of the BHZ model (dashed black curve). The shaded blue region corresponds to a simple heuristic error model based on the average fidelity 0.971 of the error mitigated experimental data [32]. This error model confirms that the comparatively large deviations of the measured Chern number that we observe are produced already from low loss in fidelity (≈3%). Insets show the distribution of experimental data on the Bloch sphere under dynamics for $M = 1$ and $M = 3$, illustrating qualitative differences of the time evolution in each of the two phases $|M| < 2$ and $|M| > 2$.

the same setup as well as the ideal result in the strong-drive limit. We find reasonable quantitative agreement with the simulations. Furthermore, the transition between different phases with different Chern number is clearly visible in the experimental data. Beyond the extracted value of the Chern number, the qualitative difference between the phases with $|M| < 2$ and $|M| > 2$ is clearly seen by considering the portion of the Bloch sphere covered under time evolution, shown inset Fig. 3. For $|M| < 2$ we observe that the state of the qubit explores the full Bloch sphere under the dynamics of Eq. (5) reflecting that the surface traced by the time dependent state has nontrivial winding around the origin and hence non-zero Chern number. When $|M| > 2$ the state of the qubit is instead restricted to either the north or south hemisphere of the Bloch sphere and does not wind around the origin and the Chern number is zero.

While overall the agreement is good, the error in the measured Chern number exceeds the error predicted by the fidelity considerably. We find that this can be explained by a simple error model, in which we take the state predicted in the ideal scenario and randomly perturb its direction on the Bloch sphere to reproduce the measured distribution of fidelities with average 0.971 [32]. Note that the perturbations at data points corresponding to different times are independent, as they correspond to different experimental runs. This perturbation translates into an error in the measured Chern number, whose standard deviation we plot as a shaded region in Fig. 3. This shows that a error rate consistent with experimental data explains the large errors in the extracted Chern number.

Extension to qubit arrays.—In view of the vast research effort in Floquet matter, the question is pertinent whether the presented scheme generalizes to several qubits. To answer this question we must be aware that the coupling between two qubits can be engineered in many ways, as one can choose between direct capacitive or inductive coupling, or indirect coupling via a resonator [37–41]. Indeed, alternative approaches have been taken by IBM (see, e.g., Ref. [42]) and Google [43], with each implementation having their own (dis-)advantages.

We consider two cases in particular. The first is when both qubit frequencies and their coupling is fixed, which is relevant for the devices developed by IBM. In this case, the coupling has to be engineered with time-dependent driving of the qubits in order to implement resonant processes to second order in the Hamiltonian [44–46]. This technique produces tuneable XZ, YZ, ZX, and ZY interactions, which are used to engineer CR gates [45,47]. Implementing a similar single-qubit driving as before, and passing into a time-dependent reference frame, we derive an effective Hamiltonian of the form [32]

$$H_{\mathrm{int}}^{(2)} = \sum_{\langle ij \rangle} g_{ij}(t) \sigma_z^{(i)} \sigma_+^{(j)} + \mathrm{H.c.} \tag{10}$$

On bipartite lattices, a (virtual) rotation of every second spin maps this to either an Ising interaction or (in general anisotropic) XY interactions, making this technique very versatile. A drawback is that the Hamiltonian (10) is

obtained to second order in the original Hamiltonian and by neglecting quickly rotating terms. It is thus an approximation and care has to be taken that all the steps in its derivation are valid. Nevertheless, these conditions can usually be fulfilled through careful choice of the driving parameters. It may further be possible to actively counteract unwanted effects from this approximation, analogous to the DRAG scheme used to improve the fidelity of digital quantum gates [8].

If tunable interactions are available and the qubits can be brought into resonance [43], the driving scheme is simplified and one readily arrives at the general spin Hamiltonian

$$H_{\text{array}}(t) = \sum_i \vec{h}^{(i)}(t) \cdot \vec{\sigma}^{(i)} + \sum_{\langle ij \rangle} g_{ij}(t)(\sigma_x^{(i)}\sigma_x^{(j)} + \sigma_y^{(i)}\sigma_y^{(j)}) \tag{11}$$

with a magnetic field along z that takes the form

$$h_z^{(i)}(t) = h_z(t) + \omega_i(t) - \omega_0, \tag{12}$$

where ω_i are the qubit frequencies and ω_0 is some arbitrarily chosen reference frequency. We note that tunable qubit frequencies feature in many implementations [48–51], but not in all [52]. In the latter case—of fixed qubit frequencies but tunable interactions—one option might be to drive each qubit with a far off-resonant drive to induce an drive-strength-dependent ac Stark shift.

When taking into account the second excited state of each qubit, the qubit array Hamiltonian (11) maps to a Bose-Hubbard model with time-dependent hopping and freely tuneable site-dependent drive and disorder. We note that the interpretation as a (time-independent) Bose-Hubbard model has enabled the experimental measurement of microscopic features of the many-body localized phase [13]. Moving to periodically varying hoppings could allow one to study many-body Floquet models and implement quench and ramp experiments from carefully prepared initial states.

Discussion.—While our experiment showcases some of the promises of analog quantum simulation with time-dependent Hamiltonians, it also highlights some of the difficulties that need to be overcome on the way. Concretely, the experimental results shown in Fig. 3 would improve with greater coherence time of the qubit, as this would allow us to reduce the modulation frequencies ω_1 and ω_2 in the Hamiltonian, which in turn would improve the strong-driving and adiabatic-modulation approximations. This is particularly important close to the topological transition at $M = 2$ where the gap closes and adiabatic evolution thus requires increasingly long timescales.

In this specific experiment, we also encountered the problem that the measured experimental signature is sensitive to even small amounts of noise. Recently, Boyers *et al.* [53] demonstrated experimental measurement of the Chern number in the same model using a nitrogen vacancy centre. They determined the Chern number by measuring the Berry curvature directly, whereas here we extract the Chern number from the topological pumping as originally proposed. As a result, they did not observe the substantial errors in the extracted Chern number that we found. Nevertheless, as we have demonstrated, the temporal topological nature of the qubit time evolution can clearly be extracted despite experimental shortcomings. With the current progress in superconducting-qubit technology, we expect that our understanding and the fidelity of available quantum computers to increase rapidly, allowing for more complex experiments, in particular with more qubits.

Going beyond (quasi)periodic driving, the capability to engineer time-dependent many-body Hamiltonians offers many exciting perspectives to investigate non-equilibrium physics. For example, ramping through a quantum phase transition might allow one to study Kibble-Zurek scaling or in general the dynamics of phase transitions such as the superfluid to Mott insulator transition [54]. Slow variation could also be used to explore adiabatic algorithms and departures from them. Many-body non-equilibrium physics is notoriously difficult to study with classical computers and this is therefore a prime area of applicability for quantum simulators. Noisy intermediate-scale quantum computers offer a versatile combination of single-site control and readout, and large enough system sizes, and thus promise to support and complement analytical and computational approaches to understand many-body nonequilibrium physics. As we have demonstrated with the single-qubit experiment, this is a realistic outlook.

All of the data presented in this Letter, along with the python code used to generate these data and the figures in this Letter, can be found in a public repository [55].

D. M. acknowledges funding from ERC Advanced Grant QUENOCOBA under the EU Horizon 2020 program (Grant Agreement No. 742102). A. S. was supported by the European Research Council (ERC) under the European Union's Horizon 2020 research and innovation program (grant agreement No. 771537), and in the latter stages of this work by a Research Fellowship from the Royal Commission for the Exhibition of 1851. The views expressed are those of the authors and do not reflect the official policy or position of IBM or the IBM Quantum Experience team.

[*] These authors contributed equally to this work.

[1] J. Preskill, Quantum computing in the NISQ era and beyond, Quantum **2**, 79 (2018).

[2] M. A. Nielsen and I. L. Chuang, *Quantum Computation and Quantum Information* (Cambridge University Press, Cambridge, 2010).

[3] S. Lloyd, Universal quantum simulators, Science **273**, 1073 (1996).

[4] A. Smith, M. S. Kim, F. Pollmann, and J. Knolle, Simulating quantum many-body dynamics on a current digital quantum computer, npj Quantum Inf. **5**, 106 (2019).

[5] F. Tacchino, A. Chiesa, S. Carretta, and D. Gerace, Quantum computers as universal quantum simulators: State-of-art and perspectives, Adv. Quantum Technol. **3**, 1900052 (2020).

[6] A. Chiesa, F. Tacchino, M. Grossi, P. Santini, I. Tavernelli, D. Gerace, and S. Carretta, Quantum hardware simulating four-dimensional inelastic neutron scattering, Nat. Phys. **15**, 455 (2019).

[7] F. Arute *et al.*, Observation of separated dynamics of charge and spin in the Fermi-Hubbard model, arXiv:2010.07965.

[8] P. Krantz, M. Kjaergaard, F. Yan, T. P. Orlando, S. Gustavsson, and W. D. Oliver, A quantum engineer's guide to superconducting qubits, Appl. Phys. Rev. **6**, 021318 (2019).

[9] J. I. Cirac and P. Zoller, Goals and opportunities in quantum simulation, Nat. Phys. **8**, 264 (2012).

[10] S. Schmidt and J. Koch, Circuit QED lattices: Towards quantum simulation with superconducting circuits, Ann. Phys. (Berlin) **525**, 395 (2013).

[11] P. Roushan *et al.*, Chiral ground-state currents of interacting photons in a synthetic magnetic field, Nat. Phys. **13**, 146 (2017).

[12] P. Roushan *et al.*, Spectroscopic signatures of localization with interacting photons in superconducting qubits, Science **358**, 1175 (2017).

[13] B. Chiaro *et al.*, Direct measurement of non-local interactions in the many-body localized phase, arXiv:1910.06024.

[14] Q. Guo, C. Cheng, Z.-H. Sun, Z. Song, H. Li, Z. Wang, W. Ren, H. Dong, D. Zheng, Y.-R. Zhang, R. Mondaini, H. Fan, and H. Wang, Observation of energy-resolved many-body localization, Nat. Phys. **17**, 234 (2021).

[15] Y. Yanay, J. Braumüller, S. Gustavsson, W. D. Oliver, and C. Tahan, Two-dimensional hard-core Bose–Hubbard model with superconducting qubits, npj Quantum Inf. **6**, 58 (2020).

[16] I. Martin, G. Refael, and B. Halperin, Topological Frequency Conversion in Strongly Driven Quantum Systems, Phys. Rev. X **7**, 041008 (2017).

[17] B. A. Bernevig, T. L. Hughes, and S.-C. Zhang, Quantum spin hall effect and topological phase transition in HgTe quantum wells, Science **314**, 1757 (2006).

[18] P. J. D. Crowley, I. Martin, and A. Chandran, Topological classification of quasiperiodically driven quantum systems, Phys. Rev. B **99**, 064306 (2019).

[19] F. Nathan, G. Refael, M. S. Rudner, and I. Martin, Quantum phase-locking and frequency down-conversion in a driven cavity-qubit system, Phys. Rev. Research **2**, 043411 (2020).

[20] S. Körber, L. Privitera, J. C. Budich, and B. Trauzettel, Interacting topological frequency converter, Phys. Rev. Research **2**, 022023(R) (2020).

[21] Y. Baum and G. Refael, Setting Boundaries with Memory: Generation of Topological Boundary States in Floquet-Induced Synthetic Crystals, Phys. Rev. Lett. **120**, 106402 (2018).

[22] T. Alexander, N. Kanazawa, D. J. Egger, L. Capelluto, C. J. Wood, A. Javadi-Abhari, and D. C. McKay, Qiskit pulse: Programming quantum computers through the cloud with pulses, Quantum Sci. Technol. **5**, 044006 (2020).

[23] A. Eckardt, Colloquium: Atomic quantum gases in periodically driven optical lattices, Rev. Mod. Phys. **89**, 011004 (2017).

[24] T. Oka and S. Kitamura, Floquet engineering of quantum materials, Annu. Rev. Condens. Matter Phys. **10**, 387 (2019).

[25] T. Ozawa and H. M. Price, Topological quantum matter in synthetic dimensions, Nat. Rev. Phys. **1**, 349 (2019).

[26] T. Ozawa, H. M. Price, A. Amo, N. Goldman, M. Hafezi, L. Lu, M. C. Rechtsman, D. Schuster, J. Simon, O. Zilberberg, and I. Carusotto, Topological photonics, Rev. Mod. Phys. **91**, 015006 (2019).

[27] V. Khemani, R. Moessner, and S. L. Sondhi, A brief history of time crystals, arXiv:1910.10745.

[28] C. Noh and D. G. Angelakis, Quantum simulations and many-body physics with light, Rep. Prog. Phys. **80**, 016401 (2017).

[29] I. Bloch, J. Dalibard, and S. Nascimbène, Quantum simulations with ultracold quantum gases, Nat. Phys. **8**, 267 (2012).

[30] J. Koch, T. M. Yu, J. Gambetta, A. A. Houck, D. I. Schuster, J. Majer, A. Blais, M. H. Devoret, S. M. Girvin, and R. J. Schoelkopf, Charge-insensitive qubit design derived from the Cooper pair box, Phys. Rev. A **76**, 042319 (2007).

[31] M. Kjaergaard, M. E. Schwartz, J. Braumüller, P. Krantz, J. I. Wang, S. Gustavsson, and W. D. Oliver, Superconducting qubits: Current state of play, Annu. Rev. Condens. Matter Phys. **11**, 369 (2020).

[32] See Supplemental Material at http://link.aps.org/supplemental/10.1103/PhysRevLett.126.163602 for additional derivations, simulation and experimental details, as well as more data, which includes Refs. [33,34].

[33] J. A. Smolin, J. M. Gambetta, and G. Smith, Efficient Method for Computing the Maximum-Likelihood Quantum State from Measurements with Additive Gaussian Noise, Phys. Rev. Lett. **108**, 070502 (2012).

[34] B. A. Bernevig and T. L. Hughes, *Topological Insulators and Topological Superconductors*, 1st ed. (Princeton University Press, Princeton, New Jersey, 2013).

[35] D. C. McKay, C. J. Wood, S. Sheldon, J. M. Chow, and J. M. Gambetta, Efficient Z gates for quantum computing, Phys. Rev. A **96**, 022330 (2017).

[36] J. Vovrosh, K. E. Khosla, S. Greenaway, C. Self, M. Kim, and J. Knolle, Efficient mitigation of depolarizing errors in quantum simulations, arXiv:2101.01690.

[37] A. Blais, R.-S. Huang, A. Wallraff, S. M. Girvin, and R. J. Schoelkopf, Cavity quantum electrodynamics for superconducting electrical circuits: An architecture for quantum computation, Phys. Rev. A **69**, 062320 (2004).

[38] Y.-x. Liu, L. F. Wei, J. S. Tsai, and F. Nori, Controllable Coupling between Flux Qubits, Phys. Rev. Lett. **96**, 067003 (2006).

[39] A. O. Niskanen, K. Harrabi, F. Yoshihara, Y. Nakamura, S. Lloyd, and J. S. Tsai, Quantum coherent tunable coupling of superconducting qubits, Science **316**, 723 (2007).

[40] M. S. Allman, F. Altomare, J. D. Whittaker, K. Cicak, D. Li, A. Sirois, J. Strong, J. D. Teufel, and R. W. Simmonds, rf-SQUID-Mediated Coherent Tunable Coupling between a

Superconducting Phase Qubit and a Lumped-Element Resonator, Phys. Rev. Lett. **104**, 177004 (2010).

[41] S. J. Srinivasan, A. J. Hoffman, J. M. Gambetta, and A. A. Houck, Tunable Coupling in Circuit Quantum Electrodynamics Using a Superconducting Charge Qubit with a V-Shaped Energy Level Diagram, Phys. Rev. Lett. **106**, 083601 (2011).

[42] A. Kandala, K. Temme, A. D. Córcoles, A. Mezzacapo, J. M. Chow, and J. M. Gambetta, Error mitigation extends the computational reach of a noisy quantum processor, Nature (London) **567**, 491 (2019).

[43] Y. Chen *et al.*, Qubit Architecture with High Coherence and Fast Tunable Coupling, Phys. Rev. Lett. **113**, 220502 (2014).

[44] G. S. Paraoanu, Microwave-induced coupling of superconducting qubits, Phys. Rev. B **74**, 140504(R) (2006).

[45] C. Rigetti and M. Devoret, Fully microwave-tunable universal gates in superconducting qubits with linear couplings and fixed transition frequencies, Phys. Rev. B **81**, 134507 (2010).

[46] P. C. De Groot, J. Lisenfeld, R. N. Schouten, S. Ashhab, A. Lupaścu, C. J. Harmans, and J. E. Mooij, Selective darkening of degenerate transitions demonstrated with two superconducting quantum bits, Nat. Phys. **6**, 763 (2010).

[47] S. Sheldon, E. Magesan, J. M. Chow, and J. M. Gambetta, Procedure for systematically tuning up cross-talk in the cross-resonance gate, Phys. Rev. A **93**, 060302(R) (2016).

[48] L. DiCarlo, J. M. Chow, J. M. Gambetta, L. S. Bishop, B. R. Johnson, D. I. Schuster, J. Majer, A. Blais, L. Frunzio, S. M. Girvin, and R. J. Schoelkopf, Demonstration of two-qubit algorithms with a superconducting quantum processor, Nature (London) **460**, 240 (2009).

[49] R. Barends *et al.*, Superconducting quantum circuits at the surface code threshold for fault tolerance, Nature (London) **508**, 500 (2014).

[50] J. Kelly *et al.*, State preservation by repetitive error detection in a superconducting quantum circuit, Nature (London) **519**, 66 (2015).

[51] M. Reagor *et al.*, Demonstration of universal parametric entangling gates on a multi-qubit lattice, Sci. Adv. **4**, eaao3603 (2018).

[52] D. C. McKay, S. Filipp, A. Mezzacapo, E. Magesan, J. M. Chow, and J. M. Gambetta, Universal Gate for Fixed-Frequency Qubits via a Tunable Bus, Phys. Rev. Applied **6**, 064007 (2016).

[53] E. Boyers, P. J. D. Crowley, A. Chandran, and A. O. Sushkov, Exploring 2D Synthetic Quantum Hall Physics with a Quasiperiodically Driven Qubit, Phys. Rev. Lett. **125**, 160505 (2020).

[54] S. Braun, M. Friesdorf, S. S. Hodgman, M. Schreiber, J. P. Ronzheimer, A. Riera, M. del Rey, I. Bloch, J. Eisert, and U. Schneider, Emergence of coherence and the dynamics of quantum phase transitions, Proc. Natl. Acad. Sci. U.S.A. **112**, 3641 (2015).

[55] D. Malz and A. Smith, https://doi.org/10.5281/zenodo.4560106.